Proceedings of the ASME 2014 4th Joint US-European Fluids Engineering Division Summer Meeting and 11th International Conference on Nanochannels, Microchannels, and Minichannels
FEDSM2014
August 3-7, 2014, Chicago, Illinois, USA

FEDSM2014-21579

REACTIVE GEOCHEMICAL FLOW MODELING WITH CT SCANNED ROCK FRACTURES

Dustin Crandall
National Energy Technology Laboratory
Predictive Geosciences Division
Morgantown, West Virginia, USA 26507
Dustin.Crandall@netl.doe.gov

Hang Wen
The Pennsylvania State University
College of Earth and Mineral Sciences
University Park, Pennsylvania, USA 16801
hzw122@psu.edu

Li Li
The Pennsylvania State University
College of Earth and Mineral Sciences
University Park, Pennsylvania, USA 16801
lili@eme.psu.edu

Alexandra Hakala
National Energy Technology Laboratory
Engineered Natural Systems Division
Pittsburgh, Pennsylvania, USA 15236
Alexandra.Hakala@netl.doe.gov

ABSTRACT

Obtaining quality three-dimensional geometries of fractures in a natural medium, such as rock, is a non-trivial task. This paper describes how several geothermal fractured rocks were scanned using computed tomography (CT), the reconstruction procedure to generate the three-dimensional (3D) geometry of the fractured rock, and the methodology for isolating the fracture from the CT scan. A conversion process to capture the relevant geometric features of the fracture is then discussed. The scanned aperture distribution was then used to simulate the reactive flow and transport processes using a reactive transport code CrunchFlow. The accurate use of CT images in fluid flow models within complex structures allows detailed understanding on how the aperture distribution affects mineral dissolution and fracture property evolution during the EGS process. Our preliminary simulation results show the formation of the preferential flow in zones with larger apertures, which led to higher calcite dissolution rates and even larger aperture size over time in these zones. Because calcite only occupied 10% of the solid phase, its dissolution did not completely open up the aperture because other relatively non-reactive minerals (clay and quartz) remained. The traditional measure of mechanical aperture could not take into account the partial increase in void space in the rock matrix and underestimated the increase in average aperture. The chemical and hydraulic apertures, which explicitly take into account changes in mineral volumes in the rock matrix, relate better to the overall change in the effective permeability of the sample.

INTRODUCTION

To produce geothermal energy fluid must be extracted from the sub-surface with a high enough temperature to drive energy production equipment, typically in excess of 150-200 °C [1]. High grade hydrothermal systems have this high heat potential, permeable rock that enables fluid transmission, and a natural recharge of fluids to allow the extraction of this resource. There are limited locations that have all three of these properties, but many locations have subsurface temperatures that are large enough to provide electrical generation [1]. By creating a more permeable subsurface, enhanced or engineered geothermal systems (EGS) enable the circulation of fluids through a hot subsurface zone for energy production [2].

EGS have been studied and tested since the initial hot dry rock system concept was proposed by researchers at Los Alamos in the 1970's, culminating in the Fenton Hill hot dry rock reservoir field site [1,3]. By creating a connected fracture network within high temperature crystalline rocks, the Fenton Hill project provided field evidence that fluid pathways within low permeability formations could be engineered for the extraction of geothermal heat. Since then EGS tests have been performed worldwide with varying success [1].

The potential energy supply from EGS is quite high, conservatively estimated at $2.8(10^5)$ EJ (where 1 EJ = 10^{18} J) up to $5.6(10^6)$ EJ by Tester et al [1] assuming recovery rates of 2 to 40% of known resources in the United States alone. In order to achieve energy production anywhere near these rates, EGS systems must be created to maintain a permeable network of

fractures for the injected fluid to travel through and to collect the in-place heat.

Fractured networks in rocks are required to transmit fluids through the hot subsurface. However, natural fracture networks can reduce the geothermal gradient significantly due to vertical advection of geothermal fluids, as was observed in the EGS system at Soultz, France [4]. In addition several changes in the fracture system during the operation can modify the ability of an EGS reservoir to function. As geothermal fluids move through the reservoir and interact with the matrix rocks, geochemical reactions can dissolve certain minerals, or conversely precipitate minerals [5]. Chemical stimulations of low permeability wells in EGS fields are designed and performed to take advantage of the ability to dissolve specific minerals within the fracture network and increase permeability [6]. The changes during normal operations of an EGS fracture network also have a large impact on field productivity.

Understanding how permeability changes in fracture network over the life of an EGS field is important for project planning. Geochemical reactions can be observed on the core scale within the laboratory within relatively short time periods [7]. Numerical models to examine property changes over longer time scales and larger spatial scales are required to upscale laboratory results to meaningful values [5,8-10].

Reactive Transport Models (RTM) simulate the coupled processes of advection, dispersion / diffusion, and geochemical reactions. Reactive transport models were developed in the 1980s and have been extensively used to understand and quantify the complex interactions among various physical and (bio)geochemical processes in natural and engineered porous media [11-14]. RTMs have been used in a wide range of applications, including, for example, mineral dissolution [15-17], chemical weathering [18,19], ion exchange [20], and microbe-mediated redox reactions in heterogeneous porous media [21]. In this work, the reactive transport code CrunchFlow was used to simulate the coupled flow, transport, and geochemical reaction processes within the fractured rock sample [22-24].

For this study, computed tomography (CT) scanning was used to obtain the geometry of a fractured rock from an active geothermal field. The fractured rock will be used in experimental examinations of chemical alteration of the fracture in an upcoming experiment. Prior to that, a reactive transport simulation was carried out to understand and predict the spatial and temporal evolution of chemical alteration, porosity and permeability under the experimental conditions. The bulk of this paper reviews the techniques used to convert the 3D CT geometry to an appropriate format for these geochemical simulations. The paper also describes some preliminary modeling results on the predicted alteration of fracture properties during fluid flow.

GEOTHERMAL FIELD SAMPLES

Two samples from a well drilled adjacent to the ORMAT's Brady's Field EGS [25] were acquired for this study. Brady's Hot Springs is in the northern Hot Springs Mountains, northeast of Reno in Churchill County, Nevada. Brady's field and the nearby Desert Peak geothermal field have been studied extensively in the last several decades as EGS projects have been planned and performed in this area [25-27]. The sub-surface of the Hot Springs Mountains contain over 2 km of faulted and fractured volcanic and sedimentary rock from the Miocene which rest upon ash flow tufts and/or metamorphic basement rocks [25]. Brady's Core Hole #3 (BCH-03) was drilled near the southern edge of the ORMAT Brady's field facility to a depth of over 4880 ft (1487 m) in order to better understand the complex subsurface structure of this site.

The 2.5 in (6.35 cm) diameter cores from BCH-03 from depths of 4580 and 4788 ft (1396 and 1459 m) are shown in Figures 1 and 3 as received. These depths are similar to the depth of geothermal energy production at Brady's. Sub-cores were extracted for analysis perpendicular to the original coring direction using a standard 1 inch (2.54 cm) diameter core drill and drill press. These samples were then fractured using a CM 10 Core Master (Park Industries, St. Cloud MN) a hydraulic core splitter. The resultant fractured cores are shown in Figures 2 and 4 with a millimeter scale bar.

FIGURE 1: LEFT – AS RECEIVED BCH-03 CORE 4580. RIGHT – SUB-CORED SAMPLE BCH-03 4580 A.

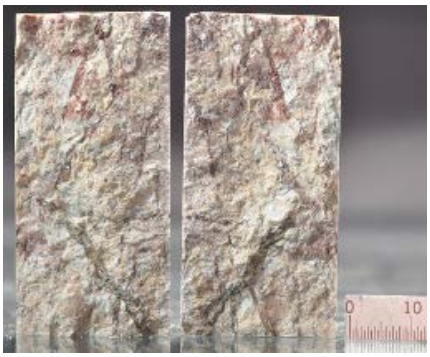

FIGURE 2: FRACTURED SUB-CORE BCH-03 4580 A WITH MM SCALE.

FIGURE 3: LEFT – AS RECEIVED BCH-03 CORE 4788. RIGHT – SUB-CORED SAMPLE BCH-03 4788 A

FIGURE 4: FRACTURED SUB-CORE BCH-03 4788 A WITH MM SCALE.

The ends of the 2.54 cm diameter sub-cores were trimmed to create flat surfaces for flow through experiments. These end cuts were pulverized for X-ray diffraction (XRD) analyses with a Rigaku Ultima-III diffractormeter. Both BCH-03 4580A and BCH-03 4788 A were mostly quartz and illite/muscovite, with over 50% of the estimated composition from the XRD analysis comprised of these two minerals. Quartz is a very stable mineral and is not expected to react in an EGS environment. Illite is a non-swelling clay and muscovite is more commonly known as mica, neither of which are expected to be highly reactive in a geothermal system either. The remaining identified minerals from the XRD analysis were minor to trace amounts of chlorite, calcite, and rutile. Calcite is the mineral that is expected to be most reactive in the presence of geothermal fluids; this fracture filling material is expected to dissolve as the reservoir temperature decreases due to cold fluid injection, altering portions of the fracture wall surfaces.

COMPUTED TOMOGRAPHY SCANNING

High resolution CT scanning was performed with a North-Star Imaging Inc. M-5000 Industrial Computed Tomography System (Industrial CT). The system was used to obtain scans with a voxel (volume pixel) size of ≈30 μm and is shown in Figure 5 with a sandstone core on the sample stage. Fractured samples BCH-03 4580A and BCH-03 4788A were placed in a Hassler style core holder (Core Lab, Tulsa OK) and a confining pressure of 100 psi (689 kPa) was applied radially to the fractured cores to ensure they were well mated during the CT scans. Scans were performed with an X-Ray voltage of 250 kV and a current of 2 μA, resulting in a focal spot size of 4 μm on the Perkin Elmer flat panel detector. The fractured samples were rotated 360° and 1440 radiograph projections of the samples were obtained, averaging 10 individual radiographs at each step. The radiographs were reconstructed using eFX software provided by North-Star Imaging. 16-bit greyscale tiff slices of the 3D reconstructed geometry were exported from eFX for further analysis with ImageJ [28]; individual tiff slices for the two fracture sub-cores are shown in Figures 6 and 8.

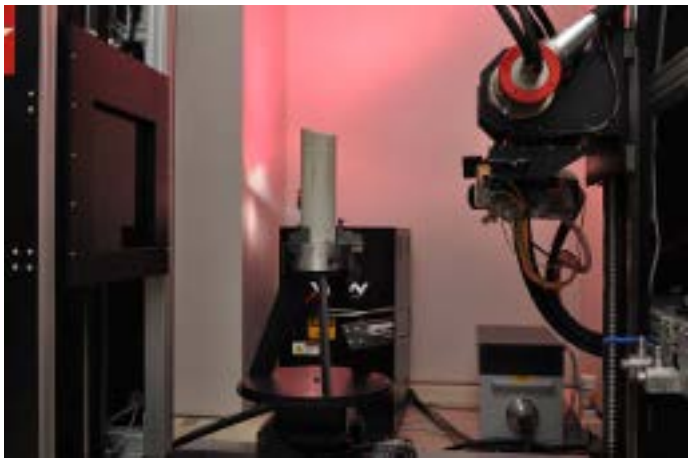

FIGURE 5: NETL'S NORTH-STAR IMAGING INDUSTRIAL CT SCANNER.

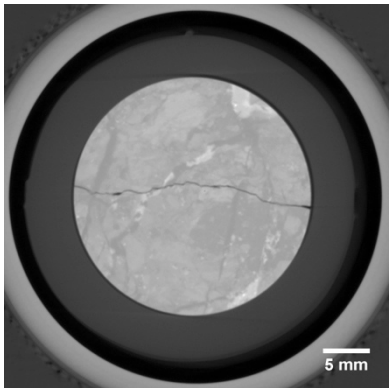

FIGURE 6: SINGLE XY CT IMAGE OF BCH-03 4580A WITHIN THE HASSLER STYLE CORE HOLDER.

FIGURE 7: ISOLATED XY SLICE OF BCH-03 4580A FRACTURE.

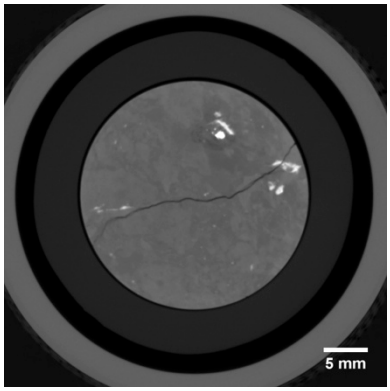

FIGURE 8: SINGLE XY CT IMAGE OF BCH-03 4788A WITHIN THE HASSLER STYLE CORE HOLDER.

FIGURE 9: ISOLATED XY SLICE OF BCH-03 4788A FRACTURE.

CONVERSION TO 2D APERTURE MAP

In order to isolate the fractures from the 3D images obtained from the CT scanning, the images must undergo a thresholding processes. As has been discussed in detail in Kutchko et al. [29], this is a non-trivial process in natural materials such as rocks or cement. Different materials are able to be distinguished visually based on the CT number (CTN) of the exported CT geometry, as can be seen in Figure 6 and 8. Lower CTN values are typically lower density material, and are visualized as darker zones, while higher CTN values are typically higher density materials and are shown as brighter zones. For example, the rubber sleeve directly around the fractured cores in Figures 6 and 8 are brighter than the low density air around the sleeve, and the composite outside of the core holder has a higher density than either of these materials so it appears as brighter. The rock matrix of the samples used here are quite heterogeneous (i.e. Figures 2 and 4), which results in a wide variety of CTN values. For the fractured rock scans these can be broadly classified, in order from highest to lowest CTN, dense minerals in the matrix (bright zones), “average” density rock matrix materials (grey zones), and air in fracture space (black zones).

When high density and low density material are adjacent to each other they may each partially fill a voxel, resulting in a CTN that is between the values of pure samples of either of the materials. This partial volume effect is well documented [30], but makes straightforward isolation of features such as fractures within rock difficult; i.e. using a single threshold value to isolate a fracture may not work well. In order to isolate the fractures used for this study, two additional steps were performed beyond a typical threshold. Two dimensional representations of the isolated fracture are shown in Figures 7 and 9. As can be seen these profiles can be discontinuous, due both to the changing geometry of the fracture and the variation in the material density surrounding the fracture.

For fracture BCH-03 4580A, an Otsu threshold technique [28] was used at a single value to isolate the fracture. As is shown in Figure 10, although the majority of this 3D volume was isolated with this technique, a large portion of the exit region of the fracture was not captured. Careful examination of the photographs of the core (Figure 2) revealed that this region corresponded with a dark green mineral on the surface of the fracture. Also, it was observed within the CT scans that this fracture was open throughout the domain. In order to account for this in the flow simulation an algorithm was written to increase the value within these ‘closed zones’, as is discussed in the aperture map generation section below.

For fracture BCH-03 4788A, an OTSU threshold technique was used twice at CTN values of 8703 and 8850 to capture the large fracture aperture locations and the smaller fracture aperture locations, respectively. A larger threshold value was needed to isolate the smaller fracture locations because the fracture voxels were partially filled with some of the rock matrix and the overall CTN value of the fracture was higher. These binary data sets were combined in 3D such that if a fracture was isolated with both thresholds, the fracture opening was confirmed. In contrast, if the fracture was not identified with the lower CTN threshold but was identified with the higher CTN threshold, an aperture equal to half of the voxel resolution was added at that location. Once these data sets were combined an ImageJ plugin [31] was used to isolate the connected fracture zones and the 3D fracture representation shown in Figure 11 was isolated.

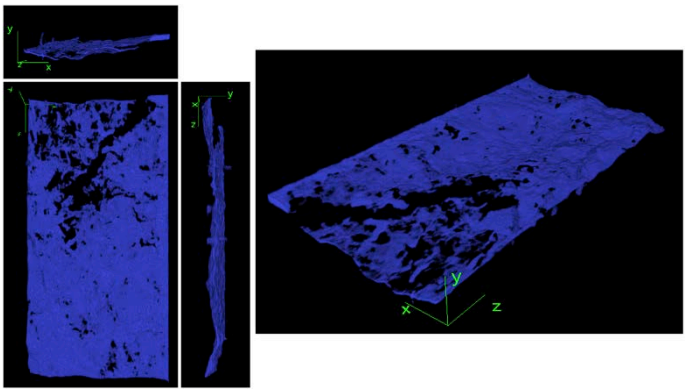

FIGURE 10: 3D RECONSTRUCTION OF FRACTURE BCH-03 4580A.

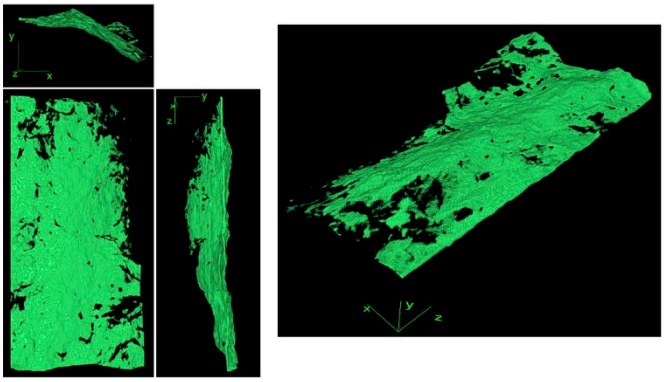

FIGURE 11: 3D RECONSTRUCTION OF FRACTURE BCH-03 4788A.

The 3D fracture geometries shown in Figures 10 and 11 are complex structures. Performing full scaled flow simulations within these domains is possible and has been performed on similar geometries previously [32,33], but this takes a great deal of computational power and rigorous meshing techniques. Since the goal of the models for this study is evaluate the changes in bulk permeability of the fracture as it evolves due to fracture-wall geochemical alterations, a simpler way of

representing the fracture flow volume was used, namely to use a localized cubic law relationship to represent the fracture volume. The 'cubic law' assumes that the flow within a fracture is similar to flow within wide, narrowly spaced parallel plates in a single direction such that the integrated Navier-Stokes equation reduces to a flow rate that is proportional to the cube of the aperture spacing of the fracture [34]. A localized cubic law relationship acknowledges this relationship, but also states that because natural rock fracture apertures vary that small subsections of the fracture can be isolated and the aperture over these smaller regions can be used to determine the resistance to flow throughout the domain. These assumptions allow for a simplified flow domain to be developed for the geochemical flow studies sought here by compressing the 3D fracture geometries shown in Figures 10 and 11 to 2D aperture maps of the fractures.

Aperture maps of the BCH-03 fractures were created by converting the isolated binary images of the fractures (i.e. Figure 7 and 9) into text images with each voxel represented by either a 0 or a 1 to represent the rock matrix or open fracture. These tab delineated text images were then loaded into a 3D matrix within FreeMat. Each column of data from the XY binary images was then summed to develop the 2D aperture maps shown in Figure 12. In this image the warm colors are larger aperture zones, with the very brightest zones equal to a local aperture of approximately 30 voxels. For the map of BCH-03 4580A, an algorithm was written to obtain the fill the zero aperture locations in with the average aperture value from the fracture zones to the left and right of the zero aperture zones. This was due to the assumption discussed earlier that the fracture was completely open, as determined by close visual examination of the CT images. The final step was multiplying the voxel scaled aperture maps by the voxel resolution of the CT scans and exporting the aperture map from FreeMat as a simple text file that could be read into the geochemical software.

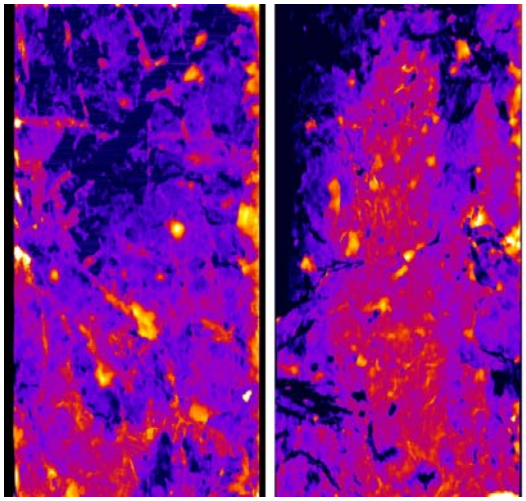

FIGURE 12: 2D FRACTURE APERTURE MAPS. LEFT BCH-03 4580A AND RIGHT BCH-03 4788A.

REACTIVE TRANSPORT MODELING

Reactive transport equation. CrunchFlow solves the advection-dispersion-reaction equations based on mass balance principles:

$$V\frac{\partial}{\partial t}(\emptyset \mathrm{C_i}) + V\nabla\cdot\{-\emptyset\mathbf{D}\nabla(\mathrm{C}_i) + \mathbf{u}\emptyset\mathrm{C}_i\} = \mathrm{R}_i \quad (\mathrm{i} = 1,2,\ldots,\mathrm{N_{tot}})$$

where V is the total volume of the targeted media (m^3), $\emptyset$ is porosity, C_i is the molal concentration of a species in solution (mol/m^3), **D** is the combined dispersion-diffusion tensor (m^2/s), **u** is the Darcian flux (m/s), R_i (mol/s) is the total reaction rate of species i in multiple reactions, and N_{tot} is the total number of independent aqueous species. The workflow of CrunchFlow is illustrated in Figure 13 [35]. For more details, we refer readers to papers by Steefel and Lasaga [35] and Steefel [36].

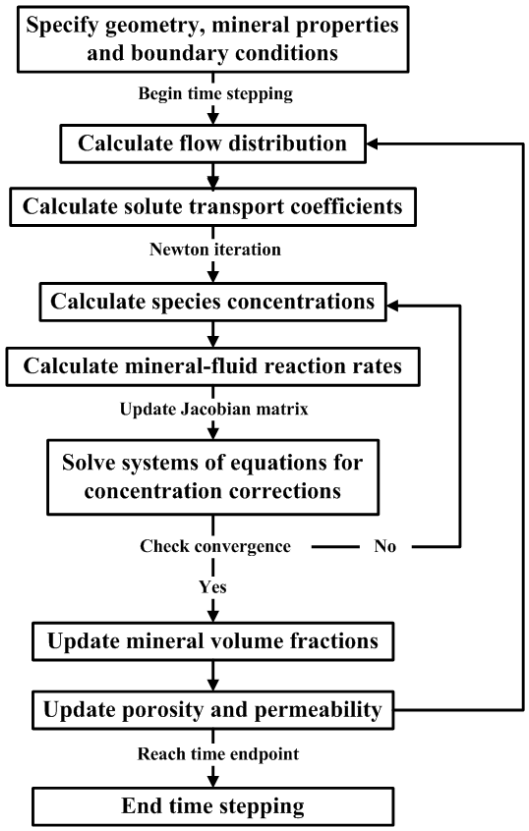

FIGURE 13: WORKFLOW OF THE REACTIVE TRANSPORT CODE CRUNCHFLOW

In this work, the rates R_i of mineral dissolution and precipitation are described using the Transition State Theory based kinetic rate laws:

$$\mathrm{R_i} = -\sum_{j=1}^{nk} \mathrm{A}_{ij}\mathrm{k}_{\mathrm{m,j}}\mathrm{a}_{\mathrm{H^+}}^{\mathrm{n_{H^+}}}\left(\prod \mathrm{a}_{\mathrm{i}}^{\mathrm{n_i}}\right)\left[1-\left(\frac{\mathrm{IAP}_j}{\mathrm{K}_{\mathrm{eq,j}}}\right)^{\mathrm{m}_{2,j}}\right]^{\mathrm{m}_{1,j}}$$

where *nk* is the total number of mineral reactions that the primary species *i* is involved in, A_{ij} is the reactive surface area (m^2) of the mineral j that involves the primary species *i*, $k_{m,j}$ is the reaction rate constant of the mineral j ($mol/(m^2 \cdot s)$), $a_{H^+}^{n_{H^+}}$

describes the effect of pH on the rate, and $a_i^{n_i}$ describes the rate dependence on activity of species *i*. The affinity term $IAP_i/K_{eq,j}$ quantifies how far away the mineral reaction *j* is from equilibrium, where IAP_j is the ionic activity product of the solution with respect to the mineral j and $K_{eq,j}$ is the equilibrium constant of the mineral reaction j. The exponents $m_{1,j}$ and $m_{2,j}$ describe the nonlinear dependencies on the affinity term and are normally obtained from experiments.

Mineral composition and reaction network. Mineral composition used in the simulation was based on experimental XRD data, including quartz (SiO_2, 50% v/v), muscovite ($KAl_2(AlSi_3O_{10}(OH)_2)$, 40% v/v) and calcite ($CaCO_3$, 10% v/v). The specific surface areas were chosen to be 0.0032, 5.8400, and 0.0037 m^2/g for quartz, muscovite, and calcite, respectively [37-39]. Because the mineral dissolution rates depend on the detailed multi-component chemistry, reaction network including aqueous complexation reactions were also considered. Table 1 lists all reactions included with their reaction thermodynamics and kinetics.

TABLE 1. REACTION NETWORK, REACTION THERMODYNAMICS AND KINETICS AT 150°C

Chemical parameters	Log K_{eq}	Log k (mol/ (m^2·s))	Ref
Aqueous speciation (at equilibrium)			
$H_2O \rightleftharpoons H^+ + OH^-$	-11.63	-	EQ3/6 database [40]
$H_2CO_3^0 \rightleftharpoons H^+ + HCO_3^-$	-6.73	-	
$HCO_3^- \rightleftharpoons H^+ + CO_3^{2-}$	-10.20	-	
$CaHCO_3^+ \rightleftharpoons Ca^{2+} + HCO_3^-$	-1.71	-	
$CaCO_3(aq) \rightleftharpoons Ca^{2+} + CO_3^{2-}$	-5.00	-	
$Ca^{2+} + OH^- \rightleftharpoons CaOH^+$	2.43	-	
$H_4SiO_4(aq) \rightleftharpoons 2H^+ + H_2SiO_4^{2-}$	-21.90	-	
$H_4SiO_4(aq) \rightleftharpoons H^+ + H_3SiO_4^-$	-8.85	-	
$Al(OH)_3(aq) \rightleftharpoons Al^{3+} + 3OH^-$	-25.94	-	
$Al(OH)_3(aq) \rightleftharpoons AlOH^{2+} + 2OH^-$	-16.51	-	
$Al(OH)_3(aq) \rightleftharpoons Al(OH)_2^+ + OH^-$	-7.73	-	
$Al(OH)_3(aq) \rightleftharpoons AlO(OH)_2^- + H^+$	-5.50	-	
Mineral dissolution and precipitation reactions			
$SiO_{2(s)} + 2H_2O \rightleftharpoons H_4SiO_4^0$	-2.66	-8.48	[39, 41,42]
$CaCO_{3(s)} + H^+ \rightleftharpoons Ca^{2+} + HCO_3^-$	0.04	-0.10	[38,43]
$CaCO_{3(s)} + H_2CO_3^0 \rightleftharpoons Ca^{2+} + 2HCO_3^-$	-6.69	-2.20	
$CaCO_{3(s)} \rightleftharpoons Ca^{2+} + CO_3^{2-}$	-10.16	-4.60	
$KAl_2[AlSi_3O_{10}](OH)_{2(s)} + 10H^+ \rightleftharpoons K^+ + 3Al^{3+} + 3H_4SiO_4^0$	-0.60	-10.65	[37,44, 45]
$KAl_2[AlSi_3O_{10}](OH)_{2(s)} + 9H_2O + H^+ \rightleftharpoons K^+ + 3Al(OH)_3 + 3H_4SiO_4^0$	42.33	-12.35	
$KAl_2[AlSi_3O_{10}](OH)_{2(s)} + 7H_2O + 5OH^- \rightleftharpoons K^+ + 3Al(OH)_4^- + 3H_3SiO_4^-$	57.43	-13.35	

*Here, the values of m_1 and m_2 are 1.0 for all the mineral species.

Corresponding to the mineral composition, SiO_2 (aq), H^+, CO_2 (aq), K^+, Al^{3+} and Ca^{2+} were considered as primary species, while all other species were considered as secondary species that depend on primary species through mass action law. Initial concentrations of primary species in the fractured sample were all set as 0.0 with a pH value of 7.0. The initial porosity for the fracture and the matrix was 100% and 1.5%, respectively. The left and right boundaries had a constant hydraulic gradient, leading to a mean flow rate of 7.1E-02 ml/min. We imposed no-flux boundaries for the top and bottom boundaries that are in parallel to the main flow. The temperature was 150°C.

To understand and predict the short-term evolution of the fractured sample, the simulation was run for 30 days based on the downscaled geometry of the sample BCH-03 4788A at a resolution of 120 μm × 120 μm. The total number of grid blocks was 390 by 195. Each grid block had its own initialized local properties, including fracture aperture, mineral composition, and permeability, and therefore explicitly representing the heterogeneity of the fractured sample that is consistent with the 2D aperture map.

Local-scale Permeability at the voxel scale. As discussed previously, the local fracture in each grid block was assumed as the parallel plate fracture. Its initial intrinsic permeability (*k*) in individual blocks was obtained from the cubic law [34]:

$$k = \frac{a_{(x,y)}^3}{12d}$$

where $a_{(x,y)}$ is the local fracture aperture for each grid block, and *d* is the height of the fracture. Values of the local permeability were updated corresponding to the evolution of mineral volume fraction during the simulation.

Effective permeability of the fracture sample. The effective permeability of the fractured sample was calculated using Darcy's law as follows:

$$k_{eff} = \frac{v\,\mu}{(\Delta p/L)}$$

where *v* is the averaged flow velocity of the sample, and μ is the fluid viscosity (Pa·s), $\Delta p/L$ is the macroscopic pressure gradient (Pa/m), and L is the length of the sample in the main flow direction x.

Average aperture size at the sample scale. Three types of fracture aperture were calculated at the sample scale, including the mechanical aperture a_m, chemical aperture a_c, and hydraulic aperture a_h:

(1) Mechanical aperture a_m is the mean of the local apertures [46]:

$$a_m = < a >_{xy} = \frac{1}{Ll}\int_{y=0}^{l}\int_{x=0}^{L} a(x,y)\,dxdy$$

where $<a>_{xy}$ is the mean of the local apertures *a(x,y)* in the targeted area, and *l* is the length of the sample in the y direction perpendicular to the flow.

(2) Chemical aperture a_c was calculated from the volume change of the minerals [46]:

$$a_c = \frac{1}{A_s}\Delta V_T + a_{c0} = \frac{1}{A_s}\sum \Delta V_i + a_{c0}$$

where ΔV_T is the total change of solid volume (m^3), $A_s = L \times l$ is the surface area of the fracture wall (m^2), ΔV_i is the volume change of the mineral *i* (m^3), and a_{c0} is the initial value of chemical aperture, which is equal to the initial sample aperture

size. The chemical aperture size can be calculated at the voxel scale and at the sample scale with their corresponding values.

(3) Hydraulic aperture a_h was derived from Darcy's Law and Cubic Law, representing the permeability of the fractured sample [47]:

$$a_h = \left[\frac{12\mu Q}{l(\Delta p/L)}\right]^{\frac{1}{3}}$$

where Q is the volume flow rate (m^3/s).

PRELIMINARY RESULTS

The simulation was carried out based on the 2D aperture map of the sample BCH-03 4788A**.** The rock matrix was composed mostly of quartz and muscovite with about 10% of calcite. Calcite was the most reactive mineral of the three and its dissolution contributed to the alteration of aperture size and fracture properties. The spatial distribution of the local chemical aperture size on days 0.1, 5, 10, 30 is shown in Figure 14. The spatial distribution of the local scale permeability (k) (not shown here) evolved with the same spatial trend of local chemical aperture. The distribution on day 0.1 was essentially the initial distribution, as it can be easily compared with Figure 12. Over time, most dissolution occurred at locations with relatively large initial apertures and at the inlet of the sample. After 30 days, a zone of significantly increased aperture size developed, reflecting the preferential flow path shaped mostly by the initial distribution of the large aperture zones. The increase in aperture size was particularly large close to the inlet. This was because the Ca^{2+} concentration and pH was the lowest at the inlet, which led to the higher dissolution rates at the inlet, as shown in Figure 15.

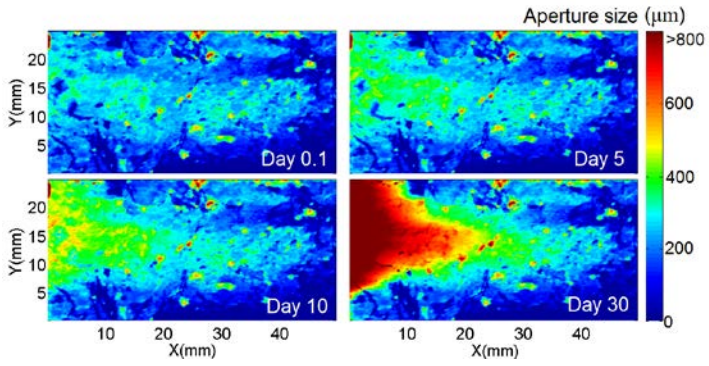

FIGURE 14: SPATIAL AND TEMPORAL EVOLUTION OF LOCAL CHEMICAL APERTURE (μM) IN FRACTURE BCH-03 4788A

Figure 15 shows the spatial evolution of pH and the calcite dissolution rate on day 0.1 and day 30. The pH varied by more than one unit, increasing from 6.4 at the inlet to 7.3 close to the fracture outlet and at the top and bottom boundary. Correspondingly, the calcite dissolution rates also varied by orders of magnitude, changing from 10^{-6} to less than 10^{-11} mol/(m^2·s). The highest reaction rates occurred at the inlet and at the larger aperture zones, similar to the patterns of the aperture size and pH. Compared with the initial time, the local calcite dissolution rate at most locations increased due to the increase in aperture size. Dissolution rates also decreased at the bottom boundary of the sample because of the significant enlargement in other parts of the inlet and the relatively less flow goes through the bottom inlet. After 30 days, highest reaction rates concentrated more at the middle part of the fractured sample.

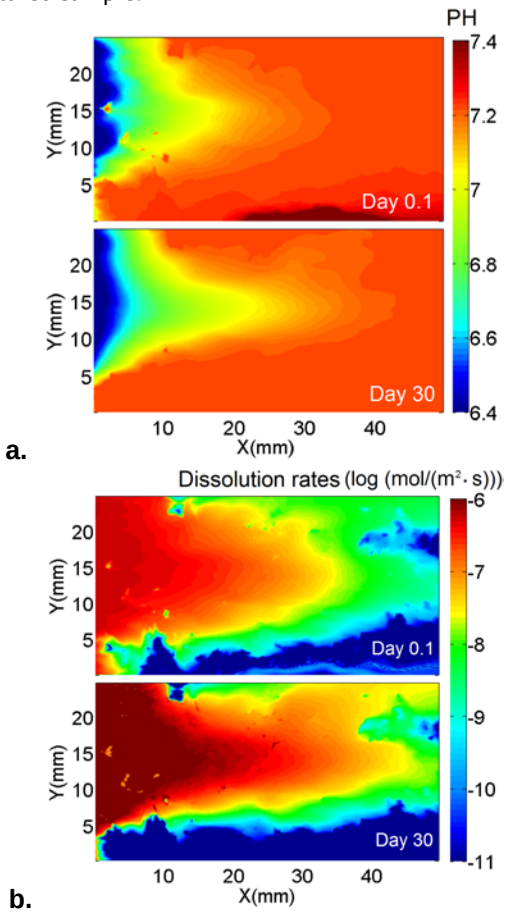

FIGURE 15: SPATIAL DISTRIBUTION OF (A) PH AND (B) THE LOGARITHMIC DISSOLUTION RATE OF CALCITE (MOL/(M^2·S)) IN BCH-03 4788A ON DAY 0.1 AND DAY 30.

The spatial distribution of the flow rates is presented in Figure 16, which shows the formation of preferable flow pathways in the fractured sample. At the initial time, the flow mainly went through the middle part of the fracture with relatively larger aperture size. Flow branches (warm color) represent the "fast" flow channel. After 30 days, the flow was still concentrated in the middle part. However, the area with higher flow rate significantly expanded compared to day 0.1. In addition, the flow field was more homogeneous with much less high flow channels compared to the initial time at the inlet half of the fracture (before 20mm in the x direction), indicating mineral dissolution has smoothed the fracture and has

decreased the fracture roughness. At the outlet part of the fracture, the flow distributions were quite similar for day 0.1 and day 30, partly due to less dissolution in the outlet portion of the fracture because of the increased pH and elevated aqueous species concentration (Figure 15a).

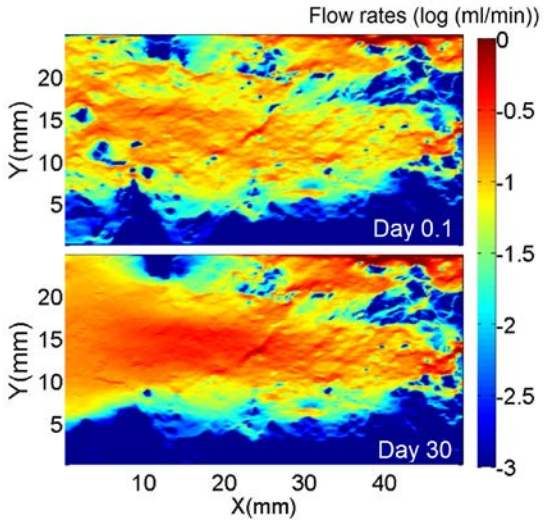

FIGURE 16: SPATIAL DISTRIBUTION OF THE LOGARITHMIC FLOW RATE (ML/MIN) IN FRACTURE BCH-03 4788A ON DAY 0.1 AND DAY 30.

Figure 17 shows the evolution of overall aperture size of the sample and the effective permeability. The chemical aperture size of the sample increased from 188.5 μm to 313.1 μm after 30 days, mostly due to calcite dissolution. The initial equivalent hydraulic aperture size of the fracture, a_h, was 160.7 μm, which is smaller than values of a_c and a_m at about 188.5 μm. Because the natural fracture was not parallel, the hydraulic aperture was not equal to other types of fracture apertures [46]. The increase in a_h is much smaller than that of the a_c. The mechanical aperture a_m was almost invariant, suggesting that the local dissolution of the calcite, about 10% of the solid phases, could not change the rock matrix into void space and therefore does not open up the fracture significantly. Because the permeability has a positive relation with the sample porosity [48], which could be approximated by the chemical aperture size, the increase of the effective permeability ratio (k_{eff}/k_{effo}) relates well with that of a_c. The increase in k_{eff} is much more significant than that of the hydraulic aperture a_h. This is largely because the permeability depends on a_h through a cubic law relationship.

DISCUSSION

Natural systems are complex and downscaling of data that can be obtained from high resolution imaging is required to understand the interactions is important to large scale processes such as EGS. By introducing some novel image processing techniques, we isolated the fractures from a series of high resolution CT scans of geothermal core for analysis. A reactive transport model based on the measured mineralogy and the imaged aperture size distribution for a fractured sample from the Brady's geothermal site was constructed with this downscaled data. Our preliminary simulation results show that larger apertures led to the preferential flow of inlet water, which led to higher calcite dissolution rates and even larger aperture size over time in these zones. Because calcite only occupied 10% of the solid phase, its dissolution did not completely open up the aperture because other relatively non-reactive minerals (clay and quartz) remained. As a result, the traditional measure of mechanical aperture could not take into account the partial increase in void space in the rock matrix and underestimates the increase in average aperture. The chemical and hydraulic apertures, which explicitly takes into account changes in mineral volumes in the rock matrix, relate better to the overall change in the effective permeability of the sample.

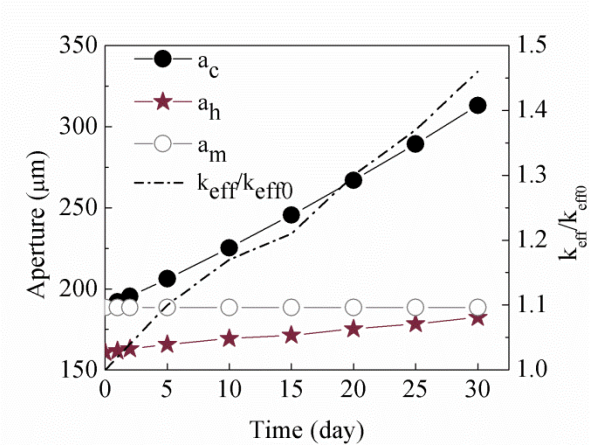

FIGURE 17: OVERALL TEMPORAL EVOLUTION OF FRACTURE APERTURE AND EFFECTIVE PERMEABILITY IN BCH-03 4788A. THE DASHED LINE FOLLOWS THE RIGHT Y AXIS AND IS FOR THE RATIO OF THE EFFECTIVE PERMEABILITY K_{EFF} OVER ITS INITIAL VALUE K_{EFF0}

ACKNOWLEDGMENTS

The authors would like to thank Bryan Tennant for the CT scanning, Karl Jarvis for the core photography, Roger Lapeer for splitting the cores, Peter Rose for providing the cores studied, and Corinne Disenhof for the XRD analysis.

NOMENCLATURE

CT – Computed Tomography
EGS – Enhanced (or Engineered) Geothermal System
EJ – Exajoule = 10^{18} J
RTM – Reactive Transport Model
IAP – Ionic Activity Product
XRD - X-Ray Diffraction
v/v – volume/volume

REFERENCES

[1] Tester, J. W., Anderson, B. J., Batchelor, A. S., Blackwell, D. D., DiPippo, R., Drake, E. M., Garnish, J., Livesay, B.,

Moore, M. C., Nichols, K., Petty, S., Toksoz, M. N., Veatch, R. W., Baria, R., Augustine, C., Murphy, E., Negraru, P., and Richards, M., 2007, "Impact of enhanced geothermal systems on US energy supply in the twenty-first century", Phil. Trans. R. Soc. A, 635, 1057-1094.

[2] Baria, R., Baugmgärtner, J., Rummel, F., Pine, R., J., and Sato, Y., 1999, "HDR/HWR reservoirs: concepts, understanding and creation", Geothermics, 28, 533-552.

[3] Duchane, D., and Brown, D., 2002, "Hot dry rock (HDR) geothermal energy research and development at Fenton Hill, New Mexico", Geo-Heat Center Bulletin, 23(4), 13-15.

[4] Genter, A., Evans, K., Cuenot, N., Fritsch, D., and Sanjuan, B., 2010, "Contribution of the exploration of deep crystalline fractured reservoir of Soultz to the knowledge of enhanced geothermal systems (EGS", C. R. Geoscience, 342, 502-516.

[5] Taron, J., and Elsworth, D., 2009, "Thermal-hydrologic-mechanical-chemical processes in the evolution of engineered geothermal reservoirs", Int. J. Rock Mechanics & Mining Sci., 46, 855-864.

[6] Rose, P., Xu, T., Kovac, K., Mella, M., and Pruess, K., 2007, "Chemical stimulation in near-wellbore geothermal formations: Silica dissolution in the presence of calcite at high temperatures and high pH", Proc. 32nd Workshop on Geothermal Reservoir Engineering, Stanford University, Stanford, CA, SGP-TR-183.

[7] Polak, A., Elsworth, D., Yasuhara, H., Grader, A. S., and Halleck, P. M., 2003, "Permeability reduction of a natural fracture under net dissolution by hydrothermal fluids", Geophys. Research Lett. 30(20) 2020.

[8] Taron, J., and Elsworth, D., 2010, "Coupled mechanical and chemical processes in engineered geothermal reservoirs with dynamic permeability", Int. J. Rock Mechanics & Mining Sci., 47, 1339-1348

[9] Gassemi, A., and Kumar, G. S., 2007, "Changes in fracture aperture and fluid pressure due to thermal stress and silica dissolution/precipitation induced by heat extraction from subsurface rocks", Geothermics, 36, 115-140.

[10] André, L., Rabemanama, V., and Vuataz, F.-D., 2006, "Influence of water-rock interactions on fracture permeability at the deep reservoir at Soultz-sous-Forêts, France", Geothermics, 35, 507-531.

[11] Steefel, C. I., and MacQuarrie, K. T. B., 1996, "Approaches to modeling of reactive transport in porous media", In Reactive Transport in Porous Media, Lichtner, P. C.; Steefel, C. I.; Oelkers, E. H., Eds. The Mineralogical Society of America: Washington, D.C., 34, 83-130.

[12] Lichtner, P. C., 1985, "Continuum Model for Simultaneous Chemical-Reactions and Mass- Transport in Hydrothermal Systems", Geochimica et Cosmochimica Acta 49(3), 779-800.

[13] Molins, S., Trebotich, D., Steefel, C. I., and Shen, C., 2012, "An investigation of the effect of pore scale flow on average geochemical reaction rates using direct numerical simulation", Water Resources Research**,** ***48***.

[14] Steefel, C. I., and Maher, K., 2009, "Fluid-rock interaction: A reactive transport approach." Reviews in Mineralogy and Geochemistry, 70, 10.2138/rmg.2009.70.11.

[15] Li, L., Salehikhoo, F., Brantley, S. L., and Heidari, P., 2014, "Spatial zonation limits magnesite dissolution in porous media", Geochimica Et Cosmochimica Acta**,** *126*(0), 555-573.

[16] Salehikhoo, F., Li, L., and Brantley, S. L., 2013, "Magnesite dissolution rates at different spatial scales: The role of mineral spatial distribution and flow velocity", Geochimica Et Cosmochimica Acta, 108(0), 91-106.

[17] Navarre-Sitchler, A., Steefel, C. I., Sak, P. B., and Brantley, S. L., 2011, "A reactive-transport model for weathering rind formation on basalt", Geochimica Et Cosmochimica Acta, 75(23), 7644-7667.

[18] Maher, K., 2010 "The dependence of chemical weathering rates on fluid residence time", Earth and Planetary Science Letters, 294(1-2), 101-110.

[19] Moore, J., Lichtner, P. C., White, A. F., and Brantley, S. L., 2012 "Using a reactive transport model to elucidate differences between laboratory and field dissolution rates in regolith", Geochimica Et Cosmochimica Acta, 93, 235-261.

[20] Singha, K., Li, L., Day-Lewis, F. D., and Regberg, A. B., 2011, "Quantifying solute transport processes: Are chemically "conservative" tracers electrically conservative?", Geophysics, 76(1), F53-F63.

[21] Li, L., Gawande, N., Kowalsky, M., Steefel, C., and Hubbard, S., 2011, "Physicochemical heterogeneity controls on uranium bioreduction rates at the field scale", Environ Sci Technol, 45, 9959 - 9966.

[22] Zhu, C., 2009, "Geochemical Modeling of Reaction Paths and Geochemical Reaction Networks", Rev Mineral Geochem, 70, 533-569.

[23] Brunet, J. P. L.; Li, L.; Karpyn, Z. T.; Kutchko, B. G.; Strazisar, B.; Bromhal, G., 2013, "Dynamic evolution of cement composition and transport properties under conditions relevant to geological carbon sequestration," Energy & Fuels, 27, 4208-4220.

[24] Steefel, C. I., DePaolo, D. J., and Lichtner, P. C., 2005, "Reactive transport modeling: An essential tool and a new research approach for the Earth sciences", Earth Planet Sc Lett, 240(3-4), 539-558.

[25] Faulds, J., Moeck, I., Drakos, P., and Zemach, E., 2010, "Structural assessment and 3D geological modeling of the Brady's geothermal area, Churchill County (Nevada, USA): A preliminary report", Proc. 35th Workshop on Geothermal Reservoir Engineering, Stanford University, Stanford, CA, SGP-TR-188.

[26] Lutz, S. J., Hickman, S., Davatzes, N., Zemach, E., Drakos, P., and Robertson-Tait, A., 2010, "Rock mechanical testing and petrologic analysis in support of well stimulation activities at the Desert Peak geothermal field, Nevada", Proc. 35th Workshop on Geothermal Reservoir Engineering, Stanford University, Stanford, CA, SGP-TR-188.

[27] Faulds, J. E., Coolbaugh, M. F., Vice, G. S., and Edwards, M. L., 2006, "Characterizing structural controls of geothermal fields in the northwestern Great Basin: A progress report", GRC Transactions, 30, 69-76.

[28] Schneider, C. A., Rasband, W. S., and Eliceiri, K. W. 2012 "NIH Image to ImageJ: 25 years of image analysis". Nature Methods 9, 671-675.
[29] Kutchko, B., Crandall, D., Gill, M., McIntyre, D., Spaulding, R., Strazisar, B., Rosenbaum, E., Haljasmaa, I., Benge, G., Cunningham, E., DeBruijn, G., and Gardner, C. 2013, "Computed Tomography and Statistical Analysis of Bubble Size Distributions in Atmospheric-Generated Foamed Cement", Technical Report No. NETL-TRS-2-2013, EPAct Technical Report Series, U.S. Department of Energy, National Energy Technology, Morgantown, WV.
[30] Keller A. A. 1997, "High resolution CAT imaging of fractures in consolidated materials", Int. J. Rock Mechanics & Mining Sci., 34(3), 358–375.
[31] Bolte, S., Cordelières, F. P., 2006, "A guided tour into subcellular colocalization analysis in light microscopy", J Microscopy, 224, 213-232.
[32] Crandall, D., Ahmadi, G., and Smith, D. H., 2009, "Conversion of a micro-CT scanned rock fracture into a useful model", Proc. FEDSM2009 Fluids Engineering Division Summer Meeting, Vail, CO, FEDSM2009-78118.
[33] Crandall, D., Ahmadi, G., and Smith, D. H., 2009, "Modeling of immiscible, two-phase flows in a natural rock fracture", Proc. FEDSM2009 Fluids Engineering Division Summer Meeting, Vail, CO, FEDSM2009-78138.
[34] Konzuk, J. S., and Kueper, B. H., 2004, "Evaluation of cubic law based models describing single-phase flow through a rough-walled fracture," Water Resour. Res., 40, W02402.
[35] Steefel, C. I., and Lasaga, A. C., 1994, "A coupled model for transport of multiple chemical-species and kinetic precipitation dissolution reactions with application to reactive Flow in single-phase hydrothermal systems, Am J Sci, 294(5), 529-592.
[36] Steefel, C. I., 2009, "CrunchFlow: software for modeling multicomponent reactive flow and transport, user's manual," Lawrence Berkeley National Laboratory.
[37] Kalinowski, B. E., and Schweda, P., 1996, "Kinetics of muscovite, phlogopite, and biotite dissolution and alteration at pH 1-4, room temperature", Geochimica Et Cosmochimica Acta, 60(3), 367-385.
[38] Talman, S., Wiwchar, B., Gunter, W., and Scarge, C., 1990, "Dissolution kinetics of calcite in the H2O–CO2 system along the steam saturation curve to 210 C", Fluid-Mineral Interactions: A Tribute to HP Eugster, 41-55.
[39] Tester, J. W., Worley, W. G., Robinson, B. A., Grigsby, C. O., and Feerer, J. L., 1994, "Correlating Quartz Dissolution Kinetics in Pure Water from 25-Degrees-C to 625-Degrees-C", Geochimica Et Cosmochimica Acta **19**58(11), 2407-2420.
[40] Wolery, T. J., Jackson, K. J., Bourcier, W. L., Bruton, C. J., Viani, B. E., Knauss, K. G., Delany, J. M., 1990. "Current Status of the EQ3/6 Software Package for Geochemical Modeling", Acs Symposium Series, 416, 104-116.
[41] Rimstidt, J. D., and Barnes, H. L., 1980, "The Kinetics of Silica-Water Reactions", Geochimica Et Cosmochimica Acta **,** 44(11), 1683-1699.
[42] Worley, W. G., Tester, J. W., and Grigsby, C. O., 1996, "Quartz dissolution kinetics from 100-200 degrees C as a function of pH and ionic strength", Aiche Journal, 42(12), 3442-3457.
[43] Plummer, L., Wigley, T., and Parkhurst, D., 1978, "The kinetics of calcite dissolution in CO_2-water systems at 5 degrees to 60 degrees C and 0.0 to 1.0 atm CO_2", American Journal of Science, 278(2), 179-216.
[44] Nagy, K. L., 1995, "Dissolution and precipitation kinetics of sheet silicates". Chemical Weathering Rates of Silicate Minerals, 31, 173-233.
[45] Knauss, K. G., and Wolery, T. J., 1989, "Muscovite Dissolution Kinetics as a Function of Ph and Time at 70-Degrees-C", Geochimica Et Cosmochimica Acta, 53(7), 1493-1501.
[46] Noiriel, C., Gouze, P., and Made, B., 2013. "3D analysis of geometry and flow changes in a limestone fracture during dissolution", J Hydrol, 486, 211-223.
[47] Watanabe, N., Hirano, N., Tsuchiya, N., 2008. "Determination of aperture structure and fluid flow in a rock fracture by high-resolution numerical modeling on the basis of a flow-through experiment under confining pressure". Water Resour Res 2008, 44, (6).
[48] Noiriel, C., Gouze, P., and Bernard, D., 2004, "Investigation of porosity and permeability effects from microstructure changes during limestone dissolution", Geophys Res Lett, 31, (24).